Article

Motor Current Signature Analysis-Based Permanent Magnet Synchronous Motor Demagnetization Characterization and Detection

Manel Krichen [1], Elhoussin Elbouchikhi [2], Naourez Benhadj [1], Mohamed Chaieb [3], Mohamed Benbouzid [4,5,*] and Rafik Neji [1]

[1] ENIS Department of Electrical Engineering, University of Sfax, Sfax 3038, Tunisia; manel.krichen@enis.tn (M.K.); naourez.benhadj@enis.tn (N.B.); rafik.neji@enis.rnu.tn (R.N.)
[2] ISEN Yncréa Ouest, UMR CNRS 6027 IRDL, 29200 Brest, France; elhoussin.elbouchikhi@isen-ouest.yncrea.fr
[3] ENICARTHAGE Department of Electrical Engineering, University of Tunis, Tunis 2035, Tunisia; Mohamed.chaieb@enicarthage.rnu.tn
[4] UMR CNRS 6027 IRDL, University of Brest, 29238 Brest, France
[5] Logistics Engineering College, Shanghai Maritime University, Shanghai 201306, China
* Correspondence: mohamed.benbouzid@univ-brest.fr

check for updates

Abstract: Neodymium-boron (NdFeB) permanent magnets (PMs) have been widely studied in the past years since they became the material of choice in permanent magnet synchronous machines (PMSMs). Although NdFeB PMs have a better energy density than other types of magnets and are cost-effective, their magnetization is very sensitive to the PMSM operating conditions, in particular temperature, where the irreversible demagnetization degree increases over time. Therefore, it is important to characterize and diagnose demagnetization at an early stage. In this context, this paper proposes a two-step analysis study dealing with both uniform and partial demagnetization. A 2D finite element method-based (FEM) approach is used for demagnetization characterization, and then a PMSM motor current signature analysis (MCSA) approach, based on fast Fourier transform (FFT), is considered where fault cases harmonics are considered as faults indices to detect demagnetization. In some situations, the proposed two-step approach achieved results that clearly allow distinguishing and characterizing demagnetization. Indeed, a local demagnetization introduces specific sub-harmonics while a uniform demagnetization leads to the current amplitude increase for a given torque.

Keywords: permanent magnet synchronous motor; demagnetization; diagnosis; fault detection; motor current signature analysis; finite element analysis

1. Introduction

The field of predictive maintenance of electric machines has become a strategic concept in all industrial production processes. Machine monitoring makes it possible to precisely diagnose potential faults to quickly act before breakage. Electric energy converters, in particular permanent magnet synchronous machines (PMSMs), are occupying an increasingly important place in industrial equipment, electric traction (electric vehicles, ships, etc.), and power conversion in renewable energy (wind turbine, alternators, etc.) due to their high efficiency, ease of manufacture, and high power and torque density [1–4]. The sensitivity of PMs to an operating temperature, their high cost, and probable demagnetization issue requires the implementation of an appropriate diagnostic technique to describe the behavior of the machine in the presence of the fault and thus characterize the demagnetization influence.

PMs are the most costly part of PMSMs [5]. They are able to easily lose their quality under several difficult running conditions giving rise to the demagnetization fault (DMF). It can be characterized as the loss of the ability to produce magnetic flux. Demagnetization can be either uniform or partial. In a uniform demagnetization case, all magnets are uniformly affected at the same time, but for a partial demagnetization only a set of magnets is impacted by the defect.

Electrical faults, mechanical stresses, thermal and environmental conditions can damage the PMs, and generate their demagnetization [6]. An armature reaction generated by the large temperatures and high currents caused by aging, physical damage, and short-circuit causes the demagnetization fault. The physical damage and the armature reaction generally induce partial demagnetization faults and aging commonly gives rise to uniform defects.

The first effect of such fault would be the deformation of the resulting magnetic flux density in the airgap. This flux perturbation gives rise to current harmonics and unbalanced magnetic pull (UMP), which creates acoustic noise. Moreover, the electromotive force (EMF) magnitude in the stator windings will be disturbed. In some incidents, broken pieces of PMs falling in the airgap may deteriorate the winding of the stator [6]. Thus, defect detection, at an early stage of growth, is important for PMSMs and leads to the prevention of huge maintenance costs [7].

Many studies have attempted to detect demagnetized magnets. There are countless papers in the literature dealing with the issue of PMs DMF diagnosis in PMSMs. A comprehensive analysis of these fault diagnosis techniques can be found in [2,8–12]. Commonly used motor fault diagnosis methods can be divided into: Model-based and signal-based fault diagnosis methods. A model-based fault diagnosis is based on residual generation by creating a motor model containing a certain fault based on physical principles [13]. Specifically, it is based on comparing the model predicted output with the actual measured output to determine whether the fault has occurred in the motor. Contrary wise, signal-based approaches require signal processing methods [14]. It is based on the physical quantities measurement on the actual system (vibration, currents, power, noise, etc.) and then extracting the faults signature using signal processing techniques. This paper is focusing on signal-based methods. Specifically, the stator currents are used as a medium for magnets faults detection and characterization, which can be used both for online and offline condition monitoring.

In this regard, researchers from the industry and academia have investigated the demagnetization fault for the purpose of ensuring a more fast and accurate diagnosis. For example, to detect a partial demagnetization fault in PMSM operating under non-stationary conditions, Wang et al. [15] presented a novel approach using the Vold-Kalman filter (VKF-OT) based on stator current tracking characteristic orders. The envelope amplitude of the fault characteristic orders is used as a fault indicator. Moreover, authors in [16] performed the VKF-OT and dynamic Bayesian network (DBN) on the torque ripple signal to detect rotor demagnetization. In [17], the Hilbert-Huang transform (HHT) technique is considered to detect DMF in PMSM by analyzing the voltage signal of a search coil. Other works calculated the varying inductances of PMSM combined with the least square (LS) method to detect DMF [18]. In [19], the 1D conventional neural network (1D CNN) on the three phase current signals is adopted in the interior PMSM to diagnose inter-turns short-circuit (ISCF) and DMF even when the two faults occur simultaneously. Furthermore, in [20], a method based on controlling the magnitude and the current angle has been proposed to detect and differentiate between DMF and ISCF. To detect and separate three different faults in PMSM; DMF, ISCF, and static eccentricity (SE), the presented work in [21] proposed a method based on using the controlled d- and q-axes voltages changes. Authors in [22] suggested the cogging torque analysis method to detect uniform demagnetization. This method has generated a proper fault diagnosis index, which can efficiently detect the defect. The carried-out work in [23] presented an analytical model of the DMF single-coil no-load EMF for PMSM. The method can not only carry out the detection and evaluation of the degree of DMF but also the recognition of the demagnetization mode and the positioning of the magnetic demagnetization pole. Low levels of DMF can be detected also in [24] by the vibration characteristics method. Xuewei et al. focused in [25] on the local demagnetization fault of permanent magnet synchronous linear motors (PMSLMs) and

carried out the accurate identification of the position and degree of faulty PMs. A fault identification process using the S-transform (ST) and particle swarm optimization–least squares support vector machine (PSO–LSSVM) is considered. The ST produces the induced EMF signal with a higher signal characteristic expression efficiency, and the PSO-LSSVM model realizes a stronger generalization capacity and greater precision in the small sample state of PMSLM faults. Experimental results prove that the method can accurately identify the PMSLM faults with a 100% recognition rate. In [26], the authors proposed a robust and efficient technique named the second-order sliding mode control strategy for tidal turbine resilience under magnet faults.

A new method for DMF recognition and classification in double-side permanent magnet synchronous linear motors (DPMSLMs) is studied in [27]. This technique is based on the time–time-transform (TT) to conduct a magnetic signal waveform transformation, and on the extreme learning machine (ELM) as a classifier to represent the DMF position, side, and severity types in detail. The effectiveness of the proposed method is verified with a prototype motor in an experimental platform.

From the discussion addressed above, an effective, non-invasive, and fast fault diagnosis technique is highly required, which may allow the preventive maintenance for the drive system of the PMSM. It is admitted that diagnosis methods based on electrical variables such as resultant magnetic flux, torque, voltage, and current are commonly applied in PMSMs.

One of the most commonly used methods to detect PM defects is the motor current signal analysis (MCSA). It is a well proven technique for the detection of mechanical and electrical faults in PMSM. The appearance of stator current components or the increase in the amplitude of some components at characteristic frequencies expresses a motor fault condition [28]. They are performed by applying fast Fourier transform (FFT) to the stator current signal to extract the signal spectrum. In a faulty case, some harmonics show up in the spectrum, which are useful to detect DMF [28]. Numerous researches have tried to detect and diagnose DMF using MCSA based on fast Fourier transform (FFT) [29]. This technique is also proposed in [30] to detect a 25% partial demagnetization fault in the interior permanent magnet generator.

Much of the current researches on PM defect detection adopting MCSA focus on the study of distinct and specific cases of demagnetization. Nevertheless, there is a demand for better understanding of how the current signal spectral patterns produced by particular PM fault scenarios diverge, and if this could be applied to efficiently recognize several PM fault types to improve the reliability of the fault detection method.

This paper presents a study using a finite element analysis (FEA) model of a PMSM operating under healthy conditions and with a PM DMF. A set of PM uniform and local demagnetization fault cases at various severity conditions are investigated. The paper's purpose is to extract the spectral signature patterns generated in the signal of the stator current in faulty cases. The focus is made on a three-phase surface-mounted PMSM, and MCSA has been chosen as the demagnetization fault detection technique. The remaining parts of the paper are organized as follows. The modeling and analysis of magnet defects under different scenarios are presented in Section 2. Then, using FEM, the resulting airgap magnetic flux density, flux linkage, stator currents, and EMFs are studied under both a uniform and partial demagnetization fault in Section 3. Section 4 is dedicated to present the current spectrum under a healthy and faulty PMSM. The obtained results are evaluated and compared to fulfill an effective procedure to detect, when possible, each of the different demagnetization fault scenarios. Section 5 concludes this paper.

2. Modeling and Analysis of Magnets Defect Signature

Permanent magnets demagnetization in PMSM is treated as a critical phenomenon in which a magnet loses its ability to generate a magnetic flux partially or totally [22,31]. Several factors can be responsible for the magnets defect such as excessive MMF and a high operating temperature.

The magnet operates at the intersection between PM demagnetization curve (second quadrant of the B–H curve) and the load line as shown in Figure 1. The motor operates at point (x) in Figure 1a

under normal load conditions. However, the operating point may be driven below the knee of the curve due to large armature currents, which produces a demagnetizing magnetomotive force (MMF). Once the operating point is brought to (x′), it does not recover its original magnetization once the demagnetizing MMF is removed. It follows the relative recoil permeability line, which is the red dotted line (line x′-y-B_r′) of Figure 1a and recovers at point (y) under normal load conditions, causing an irreversible demagnetization. Faults in the inverter or motor due to open, short-circuited switches, phases, or a failure of the stator winding insulation can increase considerably the demagnetizing MMF and lead to a PM irreversible demagnetization [8]. Consequently, the armature current must be limited to avoid an irreversible demagnetization.
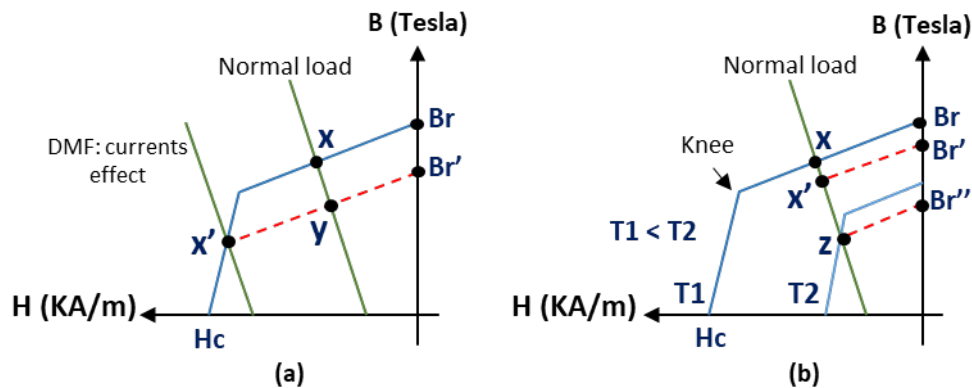

Figure 1. Irreversible demagnetization due to: (**a**) External demagnetizing magnetomotive force (MMF); (**b**) operation at a high temperature [8].

The operating point can also fall from the knee of the curve under normal conditions with a change in the operating temperature, resulting in an irreversible demagnetization. If the magnet is exposed for a long period of time to a high temperature, it can be permanently demagnetized due to changes in the metallurgical structure that affect its ability to be re-magnetized. However, if the magnet temperature exceeds the material Curie temperature, the magnetization is reduced to zero. In this case, the material can be re-magnetized if the metallurgical structure has not been affected. The residual flux density B_r and the coercivity H_c generally decrease with an increase in temperature for the NdFeB magnets. The offset of the demagnetization curve of an NdFeB magnet is illustrated in Figure 1b, when it operates at a high temperature. It can be seen that the operating point (x) falls from the knee of the curve at point (z) under normal load conditions at a high temperature T2. In this condition, the operating point is formed on the red recoil line which connects (z) and B_r″, and not on the (B–H) curve, as in the previous case. If the temperature drops to T1, the operating point is formed on the recoil line (x′-B_r′), resulting in an irreversible demagnetization.

From a fault diagnosis viewpoint, the DMF can be local or uniform. Depending on the fault-induced PM field distortion nature, distinct PM faults examined in this work are clarified by Figure 2 and categorized into two different groups: The uniform demagnetization faults and the partial demagnetization faults respectively shown in Figure 2a,b. The uniform demagnetization takes place when all existing PMs in the motor are demagnetized with the same pattern and level [29]. This fault is addressed in the following five distinct fault scenarios, which are examined based on FEM: Uniform (case 1), a symmetric (case 2) and asymmetric (case 3) reduction of the B_{PM} magnet, a symmetric (case 4) and asymmetric (case 5) reduction of the PMs arc angle (broken magnets). Similarly to the uniform demagnetization, five different situations of a local demagnetization fault are dealt with in this work by one faulty magnet out of eight: Uniform (case 6), a symmetric (case 7) and asymmetric (case 8) reduction of the B_{PM} magnet, a symmetric (case 9) and asymmetric (case 10) reduction of the PM arc angle.

In the following, a brief discussion is provided regarding the effect of these faults on the PMSM intrinsic parameters. For further development the reader can refer to [32] and the references therein.
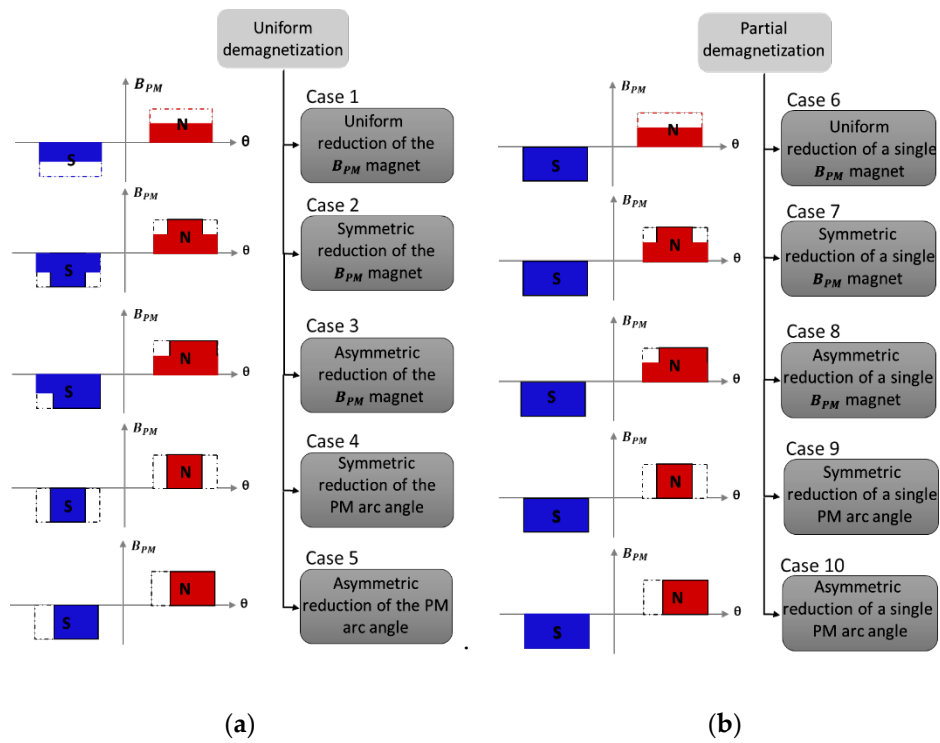
Figure 2. Permanent magnet (PM) demagnetization fault cases description: (**a**) Uniform demagnetization fault cases description; (**b**) Partial demagnetization fault cases description.

2.1. Healthy Conditions

The idealized airgap flux density generated by the rotor surface mounted PM (B_{PM}) under a normal state is shown in Figure 3.
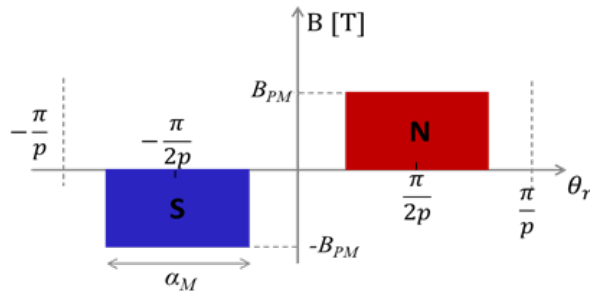

Figure 3. Ideal airgap flux density generated by the rotor surface mounted PM (B_{PM}) presented over a pole-pair pitch [29].

The normal rotor magnetic flux density distribution, B, as a function of rotor position, θ_r, for an arbitrary p-pole-pairs motor, can be described as in [29]:

$$B(\theta_r) = \sum_{n=1,3,5...}^{\infty} (B_{PM})_n \sin(np\theta_r) \tag{1}$$

with

$$(B_{PM})_n = \frac{4B_{PM}}{\pi n} \left[\sin\left(\frac{n\pi}{2}\right) \sin\left(\frac{np\alpha_M}{2}\right) \right]$$

where α_M is the arc angle of the PM in mechanical degrees, θ_r is the angular position of the rotor in mechanical degrees, p is the pole-pairs number, $(B_{PM})_n$ is the nth order PM flux density distribution Fourier coefficient, and n is the harmonic order ($n = 1, 3, 5 \dots$).

The airgap flux distribution defined in (1) is a periodic, odd function with half cycle symmetry and as such, will contain odd harmonics [29]. These, generally, will in turn create in the signal of the stator current odd harmonic components of the fundamental frequency, f_h:

$$f_h = (2k - 1)f_s \tag{2}$$

where k is an integer (k = 1, 2, 3 . . .) and f_s is the PMSM supply frequency (in our case, equal to 188.3 Hz).

2.2. Uniform Demagnetization Fault Conditions

Depending on the defect nature, a PM DMF will produce a distinct disturbance in the PM normal field distribution pattern. When a uniform DMF takes place, the PM field harmonics generated by the fault do not modify the half-cycle symmetry or the odd periodic spatial distribution of the PM field and hence only creates changes in the harmonic orders amplitude, which should exist in the airgap of a machine with healthy magnets as shown in Equation (3).

For brevity, only two of the given defect cases (case 1 and case 4) have been chosen for mathematical modeling of possible magnetic field spectral content. For example, assuming an arbitrary magnitude reduction in the airgap flux density to MB_{PM} as defined in fault case 1 or an arbitrary reduction of the PM arc angle to $X\alpha_M$ following fault case 4. Therefore, the harmonic series in (1) will be changed to (4) or (5), respectively, where X is the arc angle fault severity index and M is the flux magnitude fault severity index. X can be from 0 (total reduction of the PM arc length) to 1 (healthy PM), and M can be from 0 (total demagnetization) to 1 (healthy PM). It is clear from Equations (4) and (5) that the uniform demagnetization will not change the airgap field harmonic content. However, the existing harmonics magnitudes will change depending on the uniform fault type and severity. Hence, the possible frequencies of the stator current spectrum for a uniform demagnetization fault, f_{UD}, will be similar to those presented in the healthy motor [29]:

$$f_{UD} = f_h \tag{3}$$

$$B_{UD1}(\theta_r) = \sum_{n=1,3,5,\dots}^{\infty} \frac{4MB_{PM}}{\pi n} \left[\sin(\frac{n\pi}{2}) \sin\left(\frac{np\alpha_M}{2}\right) \right] \sin(np\theta_r) \tag{4}$$

$$B_{UD4}(\theta_r) = \sum_{n=1,3,5,\dots}^{\infty} \frac{4B_{PM}}{\pi n} \left[\sin(\frac{n\pi}{2}) \sin\left(\frac{npX\alpha_M}{2}\right) \right] \sin(np\theta_r) \tag{5}$$

Different PM faults nature or severities of PM faults would create distinct harmonics magnitude patterns in the signal of the stator current as expressed in Equations (4) and (5).

2.3. Partial Demagnetization Fault Conditions

For local faults in a single PM segment considered in cases 6–10 in Figure 2, the field distribution property of the half cycle symmetry is compromised. Therefore, with existence of any local PM damage, sub-harmonics of the fundamental frequency appear in the stator current, which are defined as in [29]:

$$f_{LD} = (1 \pm \frac{2k - 1}{p})f_s \tag{6}$$

where f_{LD} defines the fault signature of the local PM demagnetization fault, f_s is the electrical fundamental frequency, and k is an integer.

2.4. Analyses Methods

This work deals with ten cases of a demagnetization fault. To determine the behavior of PMSM under healthy and faulty conditions, a 2D FEM model is proposed. This model is developed to characterize the DMF phenomenon. Simulation results based on FEMM (finite element method magnetics) and MATLAB software help in significantly understanding the effects of these defects on intrinsic parameters of PMSMs. Indeed, the finite element method using FEMM is carried out to study and determine the electromagnetic quantities of the motor. The simulation process is based on three steps:

- Pre-processing (motor definition), which consists of providing the information necessary for the representation of the motor geometry, allows defining the mesh sizing for each section, as well as the definition of the physical properties of each material. A MATLAB script allows defining the motor geometry and materials proprieties.
- Processing, which consists of solving the magnetics problem. This step is performed by the FEMM software.
- Post-processing, which allows the computation of many local or global quantities (inductance, torque, EMF, flux linkage, currents, etc.). Specifically, it allows computing the currents spectrum in order to characterize magnets demagnetization faults.

Figure 4 presents the overall process for motor definition, simulation, and results processing using both MATLAB and FEMM.
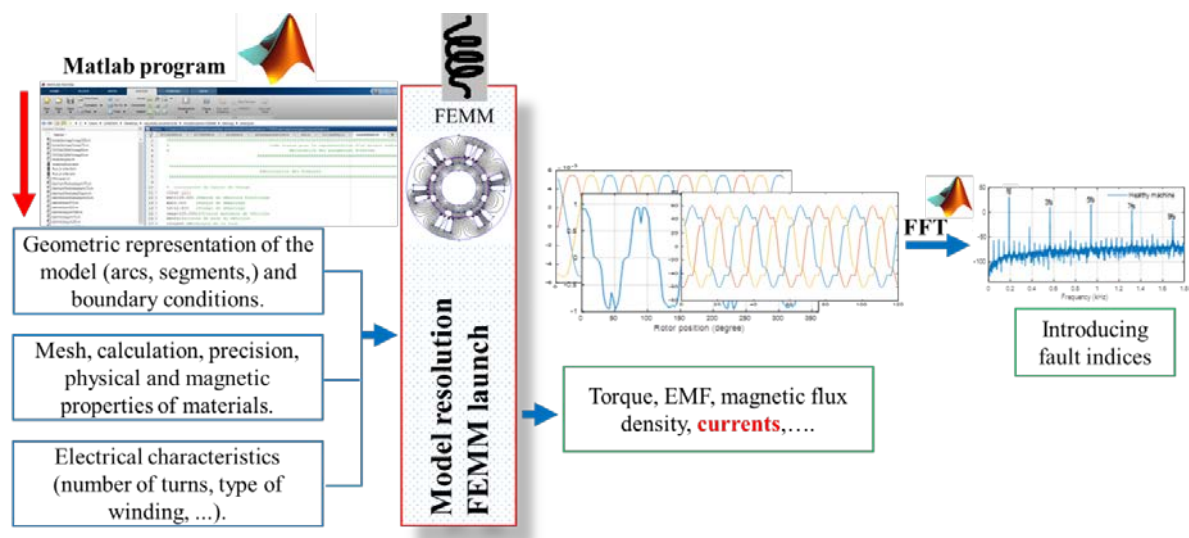

Figure 4. Permanent magnet synchronous machines (PMSMs) demagnetization fault detection procedure.

PMSM is simulated and studied under healthy and different degrees of fault severity to get an adequate data set of motor behavior under faulty conditions, which would provide the needful dataset to set up an efficient fault detection method. The resulting airgap magnetic flux density, flux linkage, stator currents, and EMFs are studied under both a uniform and partial demagnetization fault. The stator currents PSD are computed using FFT. Then, the currents spectrum under a healthy and faulty PMSM are evaluated and compared to achieve an effective procedure to detect each of the demagnetization fault scenarios. A novel frequency pattern in the DMF case is introduced, and the amplitude of sideband components (ASBCs) at frequencies obtained from the frequency pattern is used to detect distinct defect cases.

3. Finite Element Analysis Simulation Results

An electrical machines' modeling under faulty conditions is a section of the fault detection system. It is the first stage towards an electrical motors fault diagnosis. Consequently, it is mandatory to simulate the motor under several faulty cases such as DMF to analyze their characteristics and check out its performance. Thus, fast and valid models are needed to achieve this goal. FEA is commonly employed for proper modeling of DMF. It treats all the magnetic, mechanical, electrical, and geometric proprieties of motor parts under study and gives realistic and higher accuracy results, which are useful to confirm the output signals of other modeling methods. In this work, different types/degrees of DMF are simulated via the 2D-FE method.

The machine was simulated under a partial and uniform demagnetization fault. FEA simulations were carried out for the studied cases to illustrate and investigate the manifestation of the spectral patterns induced by the defect and observed for a larger set of fault severity. Different severities of defect can be studied by this model. In order to prove the effectiveness of the results, different severities of DMF from 25% to 75% have been simulated for the studied motor using the proposed model.

For cases 1, 2, 3, 6, 7, and 8, the chosen magnets material was removed with another one that has the same conductivity and relative permeability as the healthy PM but a lower magnetic flux density B_{PM} compared to the healthy magnet. A reduction of 25% ($M = 0.75$) and 75% ($M = 0.25$) of the healthy B_{PM} was considered to illustrate the uniform and local demagnetization. For the remaining cases 4, 5, 9, and 10, the damage of the magnet was presented by modifying the PM geometry accordingly for each defined PM defect scenario. A reduction of 25% ($X = 0.75$) and 75% ($X = 0.25$) of the healthy PM α_M was simulated to illustrate the reduction of the arc length magnet in the cases of the uniform and partial demagnetization.

3.1. Finite Element Study under Healthy Conditions

The analyzed machine geometry and its design parameters presented in Table A1 in Appendix A are used to develop a two-dimensional finite element motor model presented in Figure 5a.
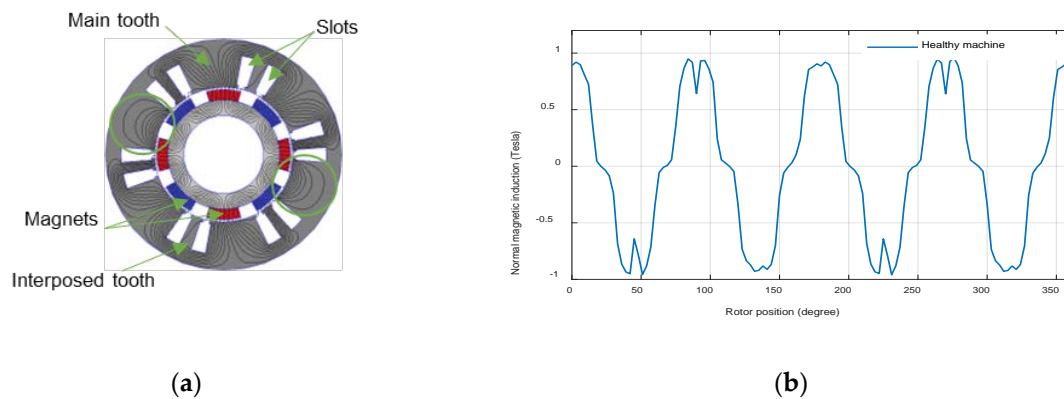

| (**a**) | (**b**) |

Figure 5. Healthy case: (**a**) Magnetic field of the healthy PMSM; (**b**) airgap magnetic flux density.

To examine the differences in the content of harmonics and sub-harmonics signal between healthy and faulty motors, it is needed to use the healthy motor as a reference pattern. This leads to directly compare machines with numerous defects and recognize the changes in the fault features location. Figure 4 presents, as a function of the rotor position, the magnetic field distribution of the PMSM and the airgap magnetic flux density obtained under healthy conditions.

The studied motor is a PMSM consisting of four pairs of poles and six main teeth, as shown in Figure 4a. Between the two main teeth, an interposed tooth is added to improve the wave form and reduce the leakage rate. Each phase winding is formed of two diametrically opposed coils whose windings are concentrated, which means that the circles of the coil are wounded directly around a

stator tooth. The field is seen to be distorted, as shown in green circles, because there are two different magnets (S and N) close to the main tooth.

3.2. Finite Element Study under Uniform Demagnetization Fault

3.2.1. Simulation Results

In order to point out the influence of uniform DMF cases defined in Figure 2, in the machine airgap magnetic field, Figures 6–10 present, as a function of the rotor position, the magnetic field distribution and the airgap magnetic flux density. Figures 11–13 present, respectively, the flux linkage, the electromotive forces (EMFs), and the current phase as a function of time, of the five uniform demagnetization cases with a 75% fault severity in comparison with healthy conditions.

- Case 1: Uniform reduction of the B_{PM} magnet

| (a) | (b) | (c) |
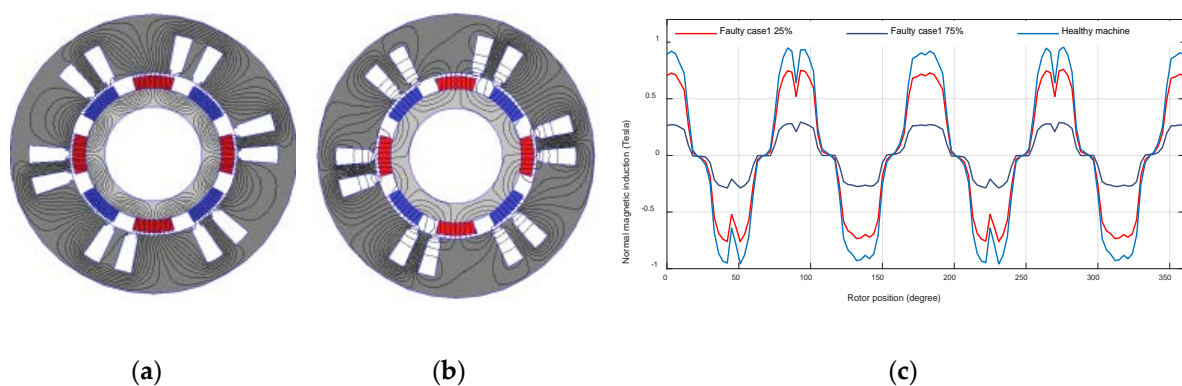
Figure 6. Faulty case 1: (**a**) Magnetic field under 25%; (**b**) magnetic field under 75%; (**c**) airgap magnetic flux density.

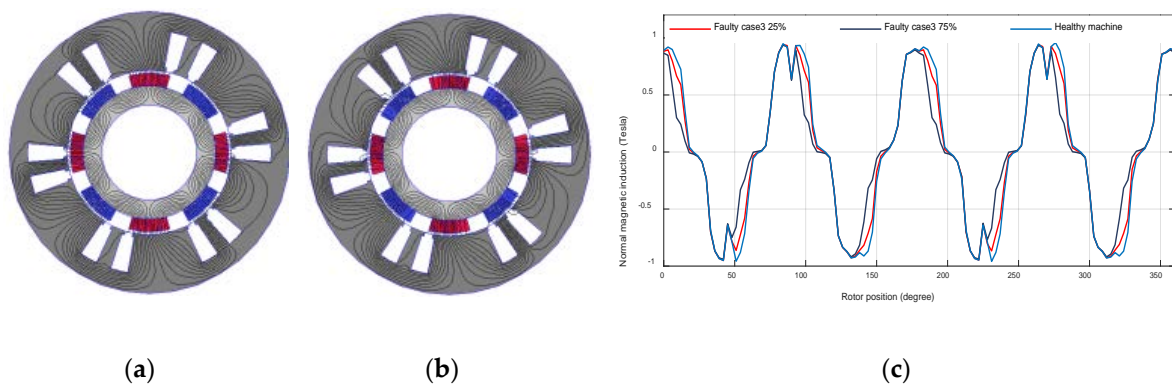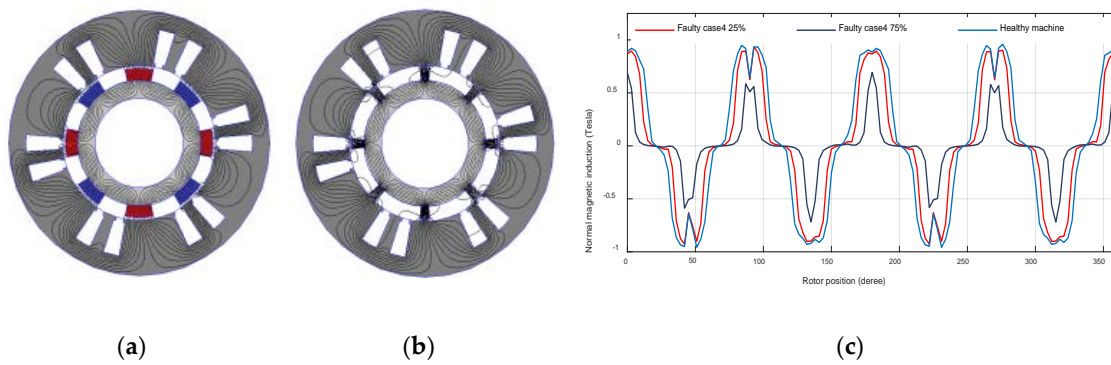- Case 2: Symmetric reduction of the B_{PM} magnet

| (a) | (b) | (c) |
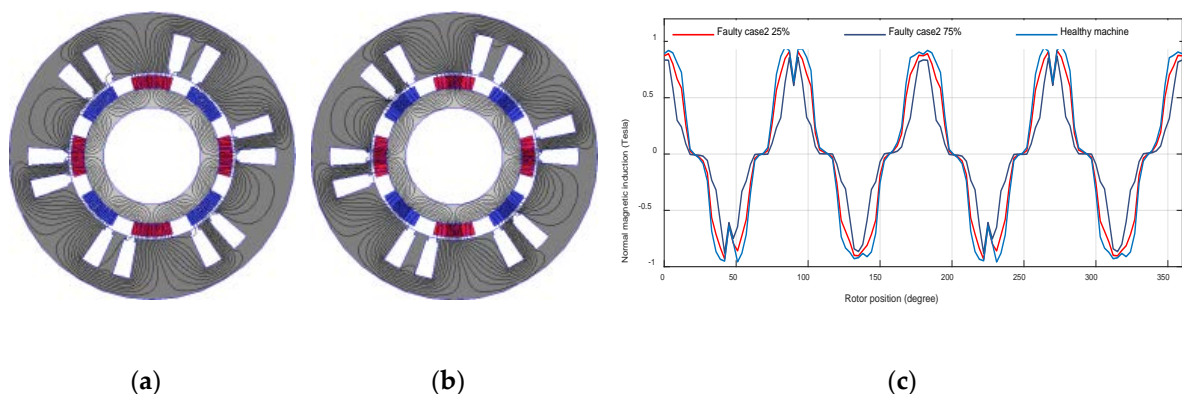
Figure 7. Faulty case 2: (**a**) Magnetic field under 25%; (**b**) magnetic field under 75%; (**c**) airgap magnetic flux density.

- Case 3: Asymmetric reduction of the B_{PM} magnet

(**a**) (**b**) (**c**)

Figure 8. Faulty case 3: (**a**) Magnetic field under 25%; (**b**) magnetic field under 75%; (**c**) airgap magnetic flux density.
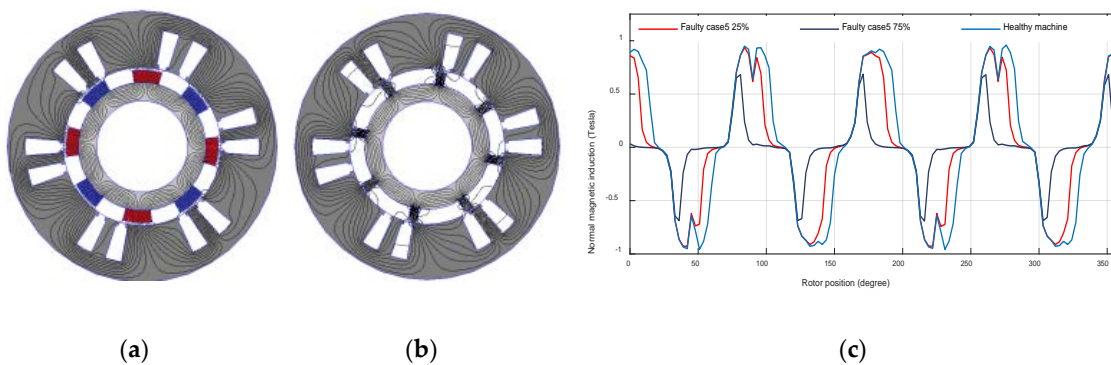
- Case 4: Symmetric reduction of the PM arc angle

(**a**) (**b**) (**c**)

Figure 9. Faulty case 4: (**a**) Magnetic field under 25%; (**b**) magnetic field under 75%; (**c**) airgap magnetic flux density.

- Case 5: Asymmetric reduction of the PM arc angle

(**a**) (**b**) (**c**)

Figure 10. Faulty case 5: (**a**) Magnetic field under 25%; (**b**) magnetic field under 75%; (**c**) airgap magnetic flux density.

- Flux linkage, EMFs, and current phase with 75% fault severity:
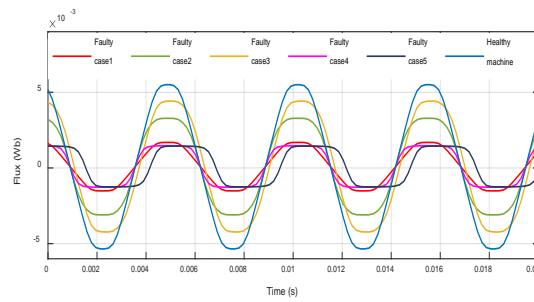
Figure 11. Flux linkage of the PMSM with 75% uniform demagnetization under different cases.
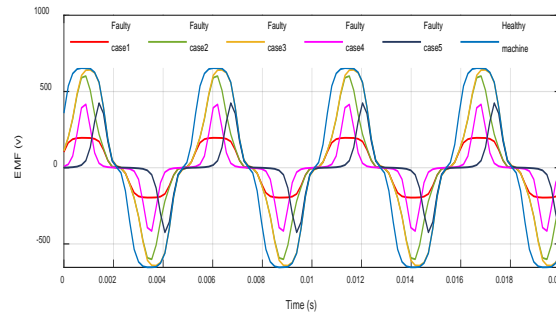

Figure 12. Electromotive forces (EMFs) of the PMSM with 75% uniform demagnetization under different cases.
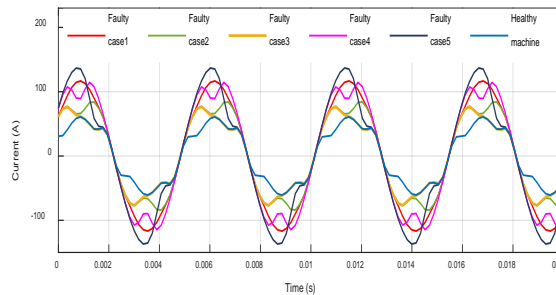

Figure 13. Current phase of the PMSM with 75% uniform demagnetization under different cases.

3.2.2. Uniform Demagnetization Fault Results Analysis

From the results presented above, demagnetization disturbs the airgap flux distribution. Since the magnets are in a uniform demagnetization, even though the faulty curves in Figure 6c revolve at the synchronous speed, it exhibits the same shape but a less magnitude value than in the healthy case. The remaining cases shown in Figures 7c, 8c, 9c and 10c disturb the airgap flux density in the shape and in the magnitude since the defect is not distributed in a balanced way in all the parts of the magnet (symmetric and asymmetric defect).

The obtained result for the symmetric reduction of the B_{PM} magnet case in all the rotor poles is given in Figure 7c. In this case, the same appearance was obtained as the healthy case but the widths of the sinusoids are reduced symmetrically. On the other hand, in case 3, an asymmetric reduction of the B_{PM} magnet, presented in Figure 8c, the widths of the sinusoids are reduced asymmetrically since the defect is distributed in a balanced way in all the parts of the magnets.

The results depicted in Figures 9c and 10c, respectively, for the cases of a symmetrical (case 4) and asymmetrical (case 5) breakage in all the rotor poles indicate the same shape as the healthy case with lower amplitudes and symmetrically (case 4) and asymmetrically (case 5) reduced sinusoids widths.

The results in Figures 11–13 show, respectively, the influence of a 75% uniform demagnetization fault in the flux, EMFs, and current compared to a healthy machine. The demagnetized PMs produce less flux than healthy PMs (Figure 11), weaken the EMFs (Figure 12), and increase the current in the

windings (Figure 13) over the machine parts. It is obvious from Figure 13 that cases 1, 4, and 5 produce a very strong current unbearable for the studied machine. Consequently, it is necessary to stop the machine operation to avoid a catastrophic failure due to demagnetization defects.

3.3. Finite Element Study under Partial Demagnetization Fault

3.3.1. Simulation Results

The obtained signals of the partial demagnetized machine cases described in Figure 1, in which one out of the eight magnets is 25% and 75% demagnetized, are presented in Figures 14–21.

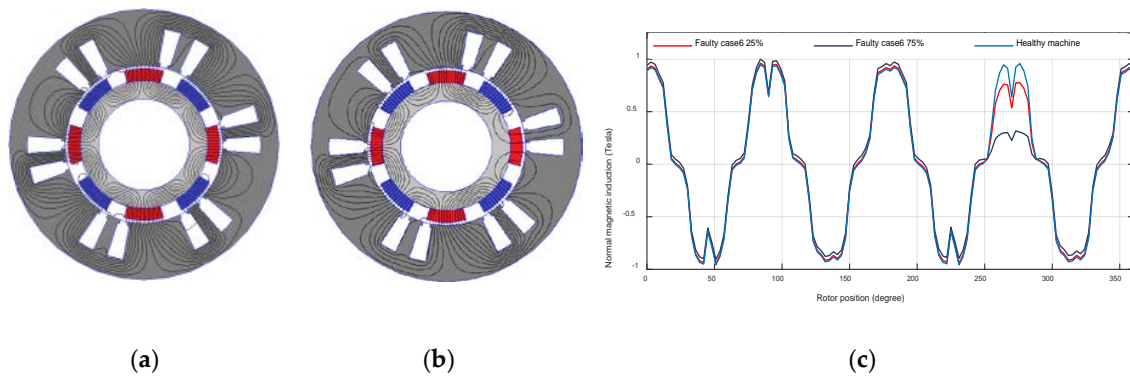- Case 6: Uniform reduction of a single B_{PM} magnet

(**a**)   (**b**)   (**c**)

Figure 14. Faulty case 6: (**a**) Magnetic field under 25%; (**b**) magnetic field under 75%; (**c**) airgap magnetic flux density.
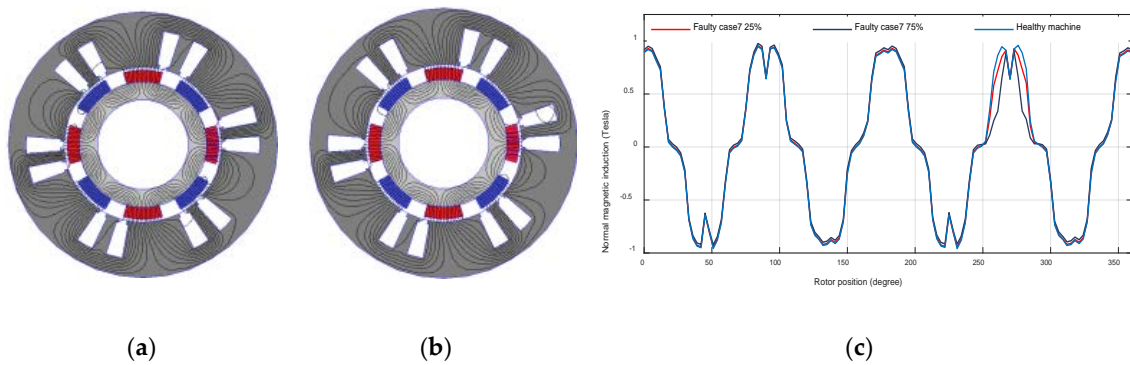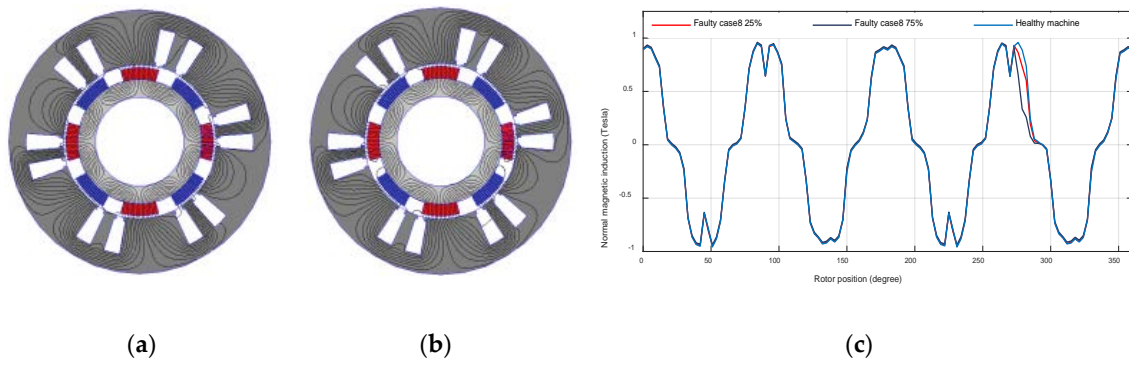
- Case 7: Symmetric reduction of a single B_{PM} magnet

(**a**)   (**b**)   (**c**)

Figure 15. Faulty case 7: (**a**) Magnetic field under 25%; (**b**) magnetic field under 75%; (**c**) airgap magnetic flux density.

- Case 8: Asymmetric reduction of a single B_{PM} magnet

(**a**)   (**b**)   (**c**)

Figure 16. Faulty case 8: (**a**) Magnetic field under 25%; (**b**) magnetic field under 75%; (**c**) airgap magnetic flux density.

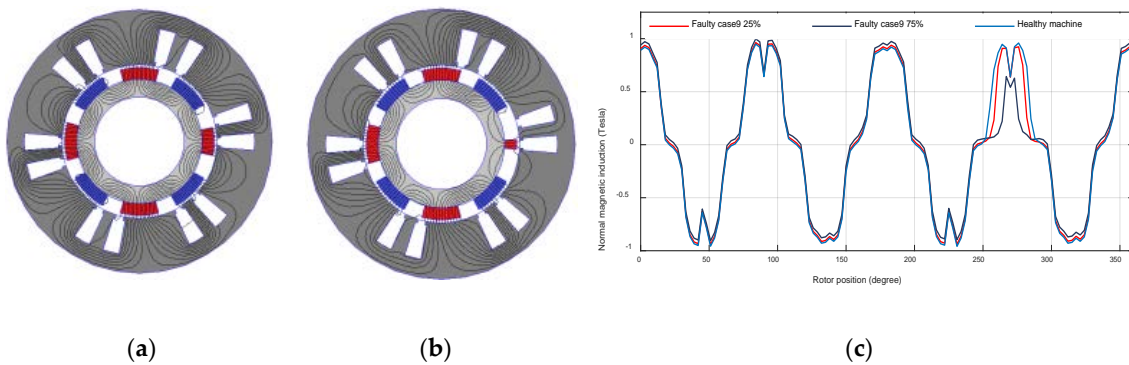- Case 9: Symmetric reduction of a single PM arc angle

(**a**)   (**b**)   (**c**)

Figure 17. Faulty case 9: (**a**) Magnetic field under 25%; (**b**) magnetic field under 75%; (**c**) airgap magnetic flux density.

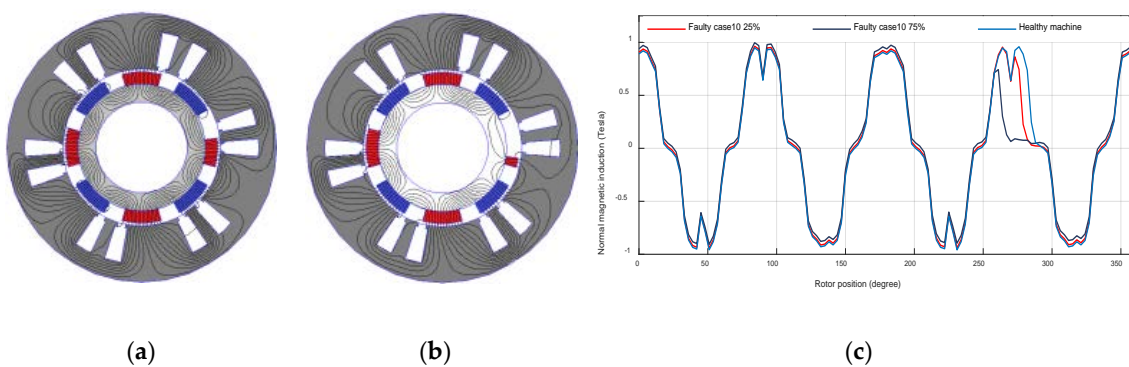- Case 10: Asymmetric reduction of a single PM arc angle

(**a**)   (**b**)   (**c**)

Figure 18. Faulty case 10: (**a**) Magnetic field under 25%; (**b**) magnetic field under 75%; (**c**) airgap magnetic flux density.

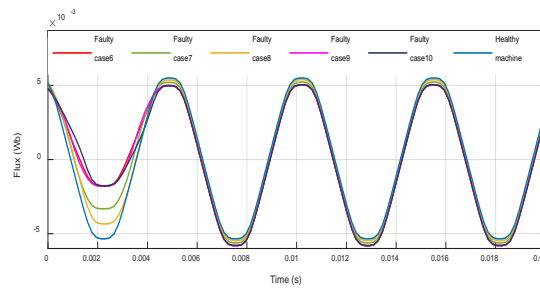- Flux linkage, EMFs, and current phase with 75% fault severity:

Figure 19. Flux linkage of the PMSM with partial demagnetization under different cases.
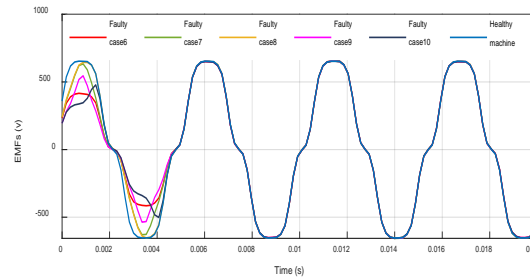

Figure 20. EMFs of the PMSM with partial demagnetization under different cases.
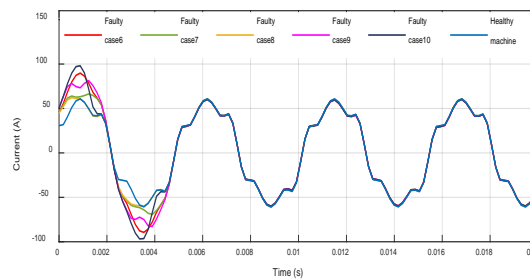

Figure 21. Current phase of the PMSM with partial demagnetization under different cases.

3.3.2. Partial Demagnetization Fault Results Analysis

In the case of a partial demagnetization fault shown in Figures 14c, 15c, 16c, 17c and 18c, a non-uniform magnetic flux density close to the damaged magnet is generated in the airgap. In addition, with the increase of fault severity, variations in the normal magnetic induction amplitude seems to be linear.

Simulation results of case 6, illustrated by Figure 14c, exhibit the same shape but less magnitude value than in the healthy case close to the damaged magnet at the rotor angular position [255 285]°.

The obtained results for the symmetric reduction of a single B_{PM} magnet case in the rotor pole S at the rotor angular positions [255 264]° and [276 285]°, are given in Figure 15c. In this case, we observe the same shape as the healthy case with symmetric reduced sinusoids widths except in the part where the magnet is damaged. On the other hand, in case 8, an asymmetric reduction of a single B_{PM} magnet at the rotor angular position [276 285]°, presented in Figure 16c, the width of the sinusoid is asymmetrically reduced.

The symmetrical breakage defined by case 9 for different degrees of severity is shown in Figure 17c. A symmetric breakage of $\frac{1}{4}$ of the magnet (25% severity degree), at the rotor angular positions [255 258.75]° and [281.25 285]°, and of $\frac{3}{4}$ (75% severity degree) of the magnet, at the rotor angular positions [255 266.25]° and [273.75 285]° have been considered. The obtained results indicate the same shape as the healthy case with less magnitude value and the sinusoids widths are symmetrically reduced close to the rotor position where the defect is introduced.

The asymmetric breakage defined by case 10 for different degrees of severity is shown in Figure 18c. An asymmetric breakage of $\frac{1}{4}$ of the magnet (25% severity degree), at the rotor angular

position [277.5 285]°, and of $\frac{3}{4}$ (75% severity degree) of the magnet, at the rotor position [262.5 285]° have been studied. The obtained results indicate the same shape as the healthy case with less magnitude value and the sinusoids widths are asymmetrically reduced close to the rotor position where the defect is achieved.

Results in Figures 19–21 show the influence of a 75% partial demagnetization fault in the flux linkage, EMFs, and currents compared to a healthy machine. The DMF effect on the motor is very severe. The defective PM produces less flux linkage than a healthy PM (Figure 19), reduces the EMFs (Figure 20), and leads to higher currents flowing in the machine windings (Figure 21) (notably cases 6, 9, and 10), which may weaken the winding insulation and affect the machine performance and parameters. These signals have the same shape and the same amplitude except for the poles affected by the partial demagnetization fault.

4. Spectral Analysis of PMSM under Different Demagnetization Fault Cases

PMSM is simulated and studied under healthy and different degrees of magnets fault severity. The three-phase stator currents in the abc reference frame are obtained from simulation results for further processing. FFT is used to compute the stator currents power spectral density (PSD) and reveal the faults signature. A novel frequency pattern in the DMF case is introduced. The amplitude of sideband components (ASBCs) extracted from the frequency pattern is used to detect distinct defect cases (Figure 4). The demagnetization defect in PMSMs disturbs the airgap magnetic field and generates some harmonics in the current spectrum, which can be used to detect DMF.

This section shows the FEA results for stator current spectra obtained under normal conditions and under all faulty cases described in Figure 2. Several fault severities can be examined by this model. In order to show the proposed approach effectiveness, different severities of the DMF including 25% and 75% have been simulated for the studied motor using FEA and the proposed model.

4.1. Spectral Analysis of PMSM under Healthy Conditions

For the healthy machine operation case, Figure 22 shows simulation results for the stator current spectrum (for a bandwidth of 0–1.8 KHz).
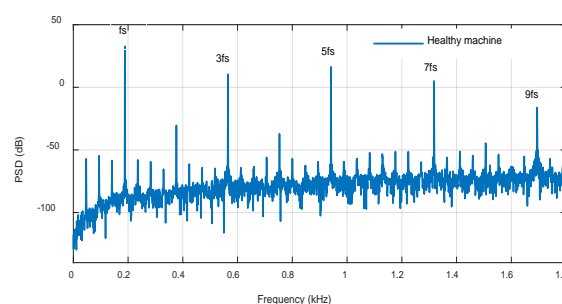

Figure 22. PMSM current spectra normalized plot under a normal case.

4.2. Harmonic Spectrum Analysis of PMSM under Uniform Demagnetization Fault Cases

4.2.1. Simulation Results

- Case 1: Uniform reduction of the B_{PM} magnet

Equation (4) expressing the spectral perturbation in an idealized PM field resulting from the defect defined in case 1 is used to extract the numerical values of flux density, presented in Figure 23d, from the airgap of the individual harmonic orders; this should generally be reflected in the current signal.
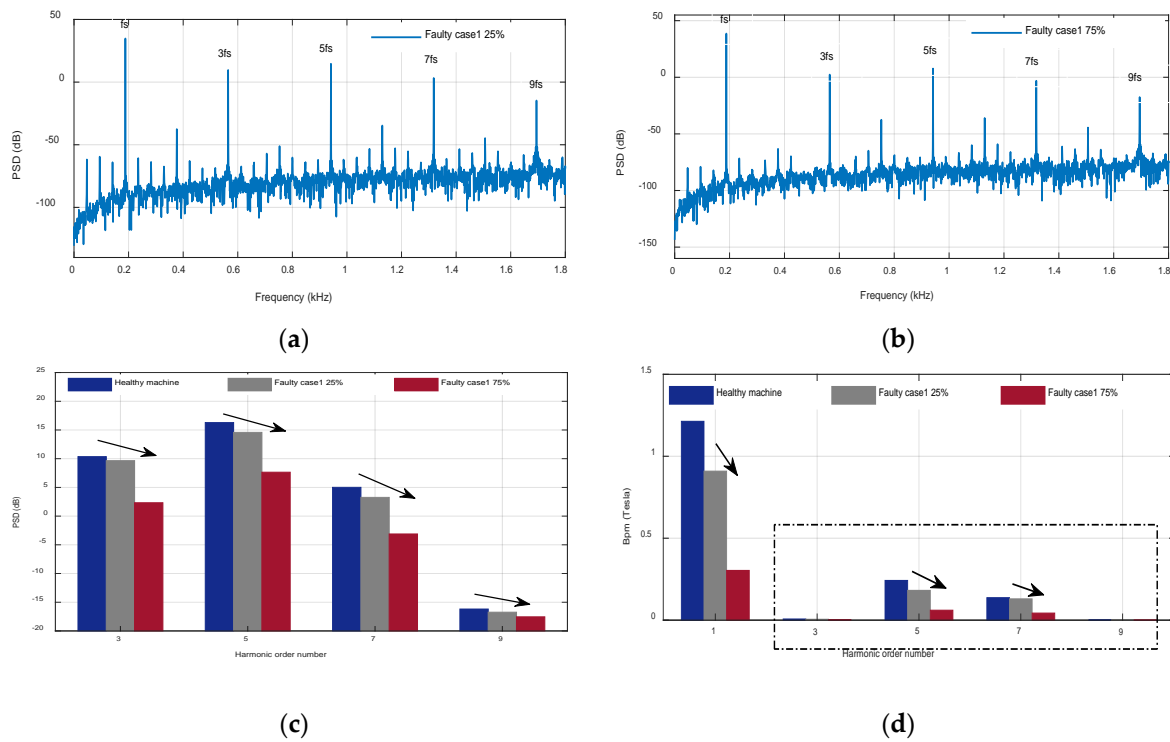
(a)

(b)

(c)

(d)

Figure 23. Faulty case 1: (**a**) PMSM current spectra normalized plot under 25%; (**b**) PMSM current spectra normalized plot under 75%; (**c**) amplitude of sideband components (ASBCs) harmonics variations; (**d**) airgap flux density distribution of harmonics magnitude variations.
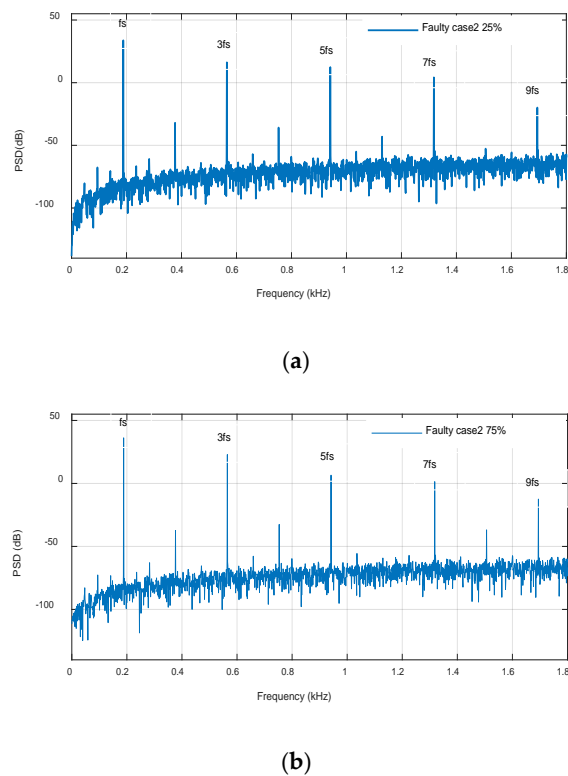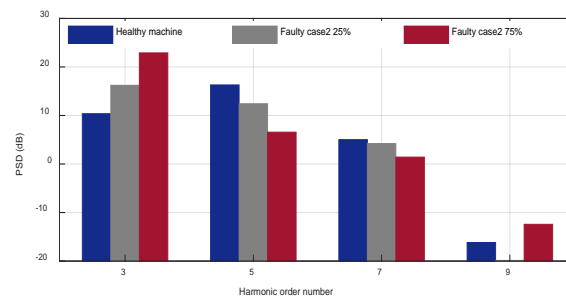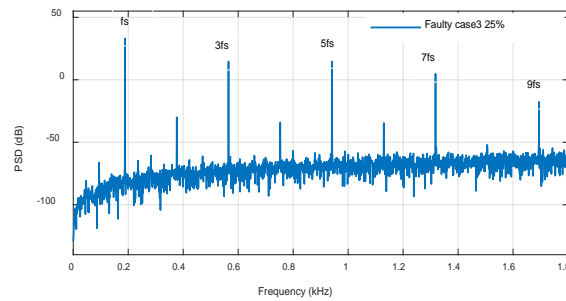
- Case 2: Symmetric reduction of the B_{PM} magnet

(a)

(b)

Figure 24. *Cont.*

(c)

Figure 24. Faulty case 2: (**a**) PMSM current spectra normalized plot under 25%; (**b**) PMSM current spectra normalized plot under 75%; (**c**) ASBCs harmonics variations.

- Case 3: Asymmetric reduction of the B_{PM} magnet

(a)

(b)

(c)

Figure 25. Faulty case 3: (**a**) PMSM current spectra normalized plot under 25%; (**b**) PMSM current spectra normalized plot under 75%; (**c**) ASBCs harmonics variations.

- Case 4: Symmetric reduction of the PM arc angle

Equation (5) expressing the spectral perturbation in an idealized PM field resulting from the defects defined in case 4 is used to extract the numerical values of flux density, presented in Figure 26d, from the airgap of the individual harmonic orders; this should generally be reflected in the current signal.
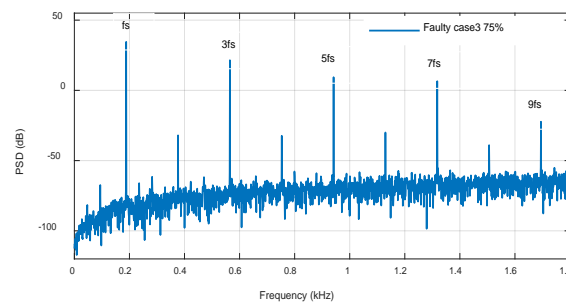

(**a**)

(**b**)

(**c**)

(**d**)

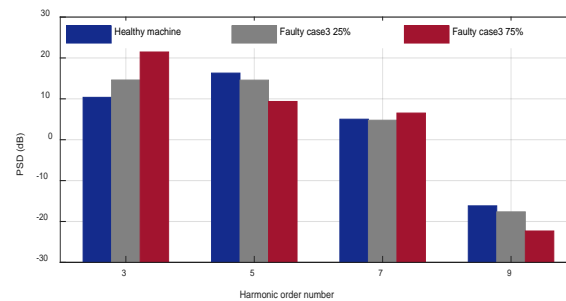**Figure 26.** Faulty case 4: (**a**) PMSM current spectra normalized plot under 25%; (**b**) PMSM current spectra normalized plot under 75%; (**c**) ASBCs harmonics variations; (**d**) airgap flux density distribution of harmonics magnitude variations.

- Case 5: Asymmetric reduction of the PM arc angle

(**a**)

Figure 27. *Cont.*
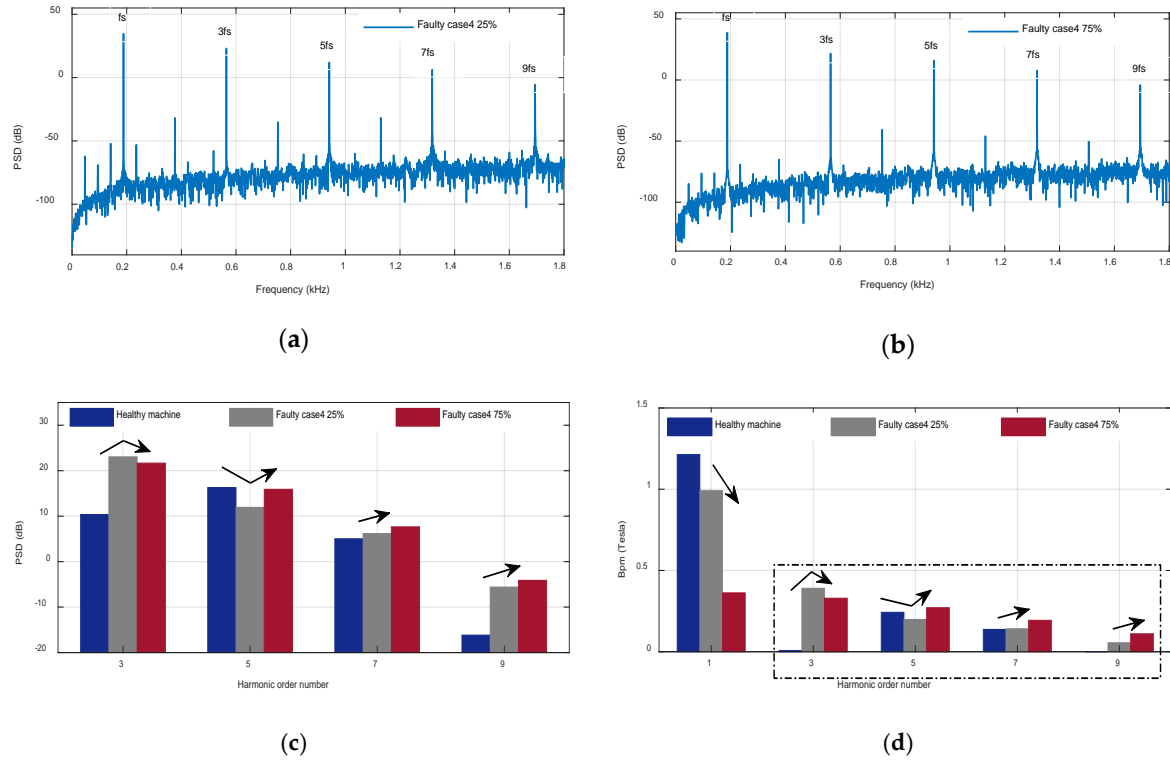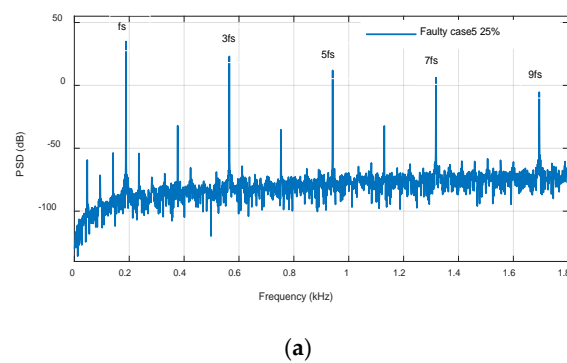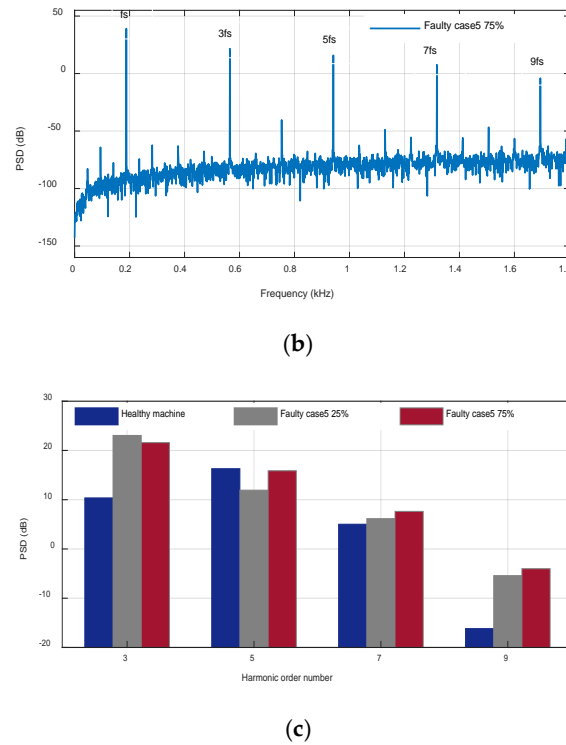
(b)

(c)

Figure 27. Faulty case 5 (**a**): PMSM current spectra normalized plot under 25%; (**b**) PMSM current spectra normalized plot under 75%; (**c**) ASBCs harmonics variations.

4.2.2. MCSA Results Analysis under Uniform Demagnetization

For the studied PMSM, the data indicate that the fault signature patterns produced by various PM fault types under uniform demagnetization show a number of similar features in the current signal.

For cases 1 to 5, as predicted in (3) and shown in Figures 23–27, the PM demagnetization generates no additional, fault specific, harmonics compared to the healthy case. However, the magnitudes of the existing harmonics in the current signal show specific modifications for different faults, indicating that an approach based on MCSA to recognize the uniform demagnetization fault would be helpful to notice any modification in the present odd current harmonics.

Therefore, the MCSA method fails to diagnose a uniform demagnetization fault. Focusing on the examined case 1 presented in Equation (4) and illustrated in Figure 23. A reduction of 25% ($M = 3/4$) and 75% ($M = 1/4$) of the healthy B_{PM} was considered to illustrate case 1.

The fault signature models predicted by the FEA in the current signal obtained from the idealized PM definitions were thus compared. This is to verify whether the fault signature models can be identified for fault diagnosis. The comparison of the results is presented in Figure 23c, where the signature model trends predicted by the FEA model are given as well as the corresponding model predictions obtained from expression (4) in Figure 23d and Table 1.

As reported by (4), for faulty case 1, the variation of the distribution of the airgap field harmonics magnitude is based on α_M value (which is constant in this fault case). The field harmonic magnitudes for a given M (fault severity) show a linear diminution with an increase of harmonic order, approximately corresponding to sin $(np\alpha_M/2)/n$. However, with an increase in fault severity (a decrease in M) individual field harmonic orders magnitudes would be expected to vary in a M sin $(np\alpha_M/2)/n$ pattern, as shown in Figure 23d and Table 1. A similar behavior can be observed in FEA predicted signature patterns in the current signal and the harmonic orders predicted by (3) are reflected in the results shown in Figure 23c and Table 1 for this case.

We can observe also that faulty case 2 (symmetric reduction of the B_{PM} magnet) and case 3 (asymmetric reduction of the B_{PM} magnet), interpreted respectively in Figure 24, Table 2 and Figure 25,

Table 3, can not be detected by MCSA method. The PM demagnetization generates no additional, fault specific, harmonics compared to the healthy case. Moreover, we can notice from Tables 2 and 3 that the MCSA method does not differentiate between symmetric (case 2) and asymmetric (case 3) reduction of the healthy B_{PM} magnet. The fault signature models predicted by the FEA in the current signal obtained in cases 2 and 3 are very close.

Focusing now on the examined case 4 presented in Equation (5) and illustrated in Figure 26. A reduction of 25% ($X = 3/4$) and 75% ($X = 1/4$) of the healthy PM α_M was studied to illustrate case 4.

The fault signature models predicted by the FEA in the current signal obtained from the idealized PM definitions were thus compared. This is to verify whether the fault signature models can be identified for fault diagnosis. The comparison of the results is presented in Figure 26c, where the signature model trends predicted by the FEA model are given as well as the corresponding model predictions obtained from expression (5) in Figure 26d and Table 4.

In the fourth faulty case, as reported by (5), the field harmonics magnitudes variation follows a sinusoidal distribution sin $(np(X\alpha_M)/2)/n$ that will depend on both the fault severity X and the harmonic order. The data shown in Figure 26d and Table 4, show that the 7th and the 9th harmonic show a uniform diminution of the magnitude with decrease of the fault severity (a reduction of α_M). A signature pattern was observed in the FEA model current spectral content predictions in Figure 26c and Table 4.

Moreover, we can notice from Figure 26, Table 4 and Figure 27, Table 5 that the MCSA method does not differentiate between symmetric (case 4) and asymmetric (case 5) reduction of the healthy PM α_M. The fault signature models predicted by the FEA in the current signal obtained in cases 4 and 5 are indistinguishable. This is predicted also from (5), which does not depend on the symmetry of the broken magnet.

Table 1. Current harmonic components comparison and airgap flux density distribution of harmonics magnitude variations due to case 1.

	Current Harmonic Components (in dB).			Airgap Flux Density Distribution of Harmonics Magnitude (in T).		
Frequency	Healthy Machine	Case 1 25%	Case 1 75%	Healthy Machine	Case 1 25%	Case 1 75%
f_s	32.65	34.78	38.56	1.213	0.909	0.303
$3f_s$	10.36	6.65	2.33	0.007	5.25×10^{-3}	1.75×10^{-3}
$5f_s$	16.29	14.59	7.65	0.242	0.181	0.060
$7f_s$	5.016	3.26	−3.10	0.137	0.129	0.043
$9f_s$	−16.18	−16.73	−17.54	7.33×10^{-4}	5.5×10^{-4}	1.83×10^{-4}

Table 2. Current harmonic components comparison due to case 2 (in dB).

Frequency	Healthy Machine	Case 2 25%	Case 2 75%
f_s	32.65	33.78	36.18
$3f_s$	10.36	16.21	22.89
$5f_s$	16.29	12.41	06.55
$7f_s$	5.016	04.20	01.41
$9f_s$	−16.18	−19.87	−12.43

Table 3. Current harmonic components comparison due to case 3 (in dB).

Frequency	Healthy Machine	Case 3 25%	Case 3 75%
f_s	32.65	33.12	34.52
$3f_s$	10.36	14.60	21.45
$5f_s$	16.29	14.57	09.35
$7f_s$	5.016	04.76	06.51
$9f_s$	−16.18	−17.65	−22.33

Table 4. Current harmonic components comparison and airgap flux density distribution of harmonics magnitude variations due to case 4.

| Frequency	Current Harmonic Components (in dB).			Airgap Flux Density Distribution of Harmonics Magnitude (in T).		
	Healthy Machine	Case 4 25%	Case 4 75%	Healthy Machine	Case 4 25%	Case 4 75%
f_s	32.65	34.63	38.60	1.213	0.990	0.362
$3f_s$	10.36	23.04	21.66	0.007	0.390	0.329
$5f_s$	16.29	11.93	15.90	0.242	0.198	0.270
$7f_s$	5.016	6.17	7.63	0.137	0.141	0.193
$9f_s$	−16.18	−5.60	−4.13	7.33×10^{-4}	0.054	0.110

Table 5. Current harmonic components comparison due to case 5 (in dB).

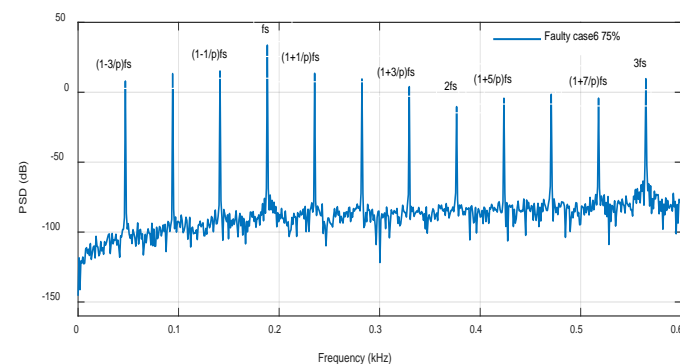| Frequency	Healthy Machine	Faulty Case 5 25%	Faulty Case 5 75%
f_s	32.65	34.89	39.07
$3f_s$	10.36	23.04	21.59
$5f_s$	16.29	11.93	15.88
$7f_s$	5.016	06.14	07.62
$9f_s$	−16.18	−05.42	−04.11

4.3. Harmonic Spectrum Analysis of PMSM under Partial Demagnetization Fault Cases

4.3.1. Simulation Results
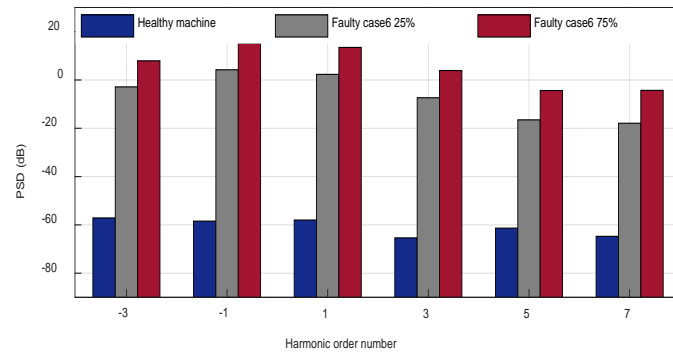
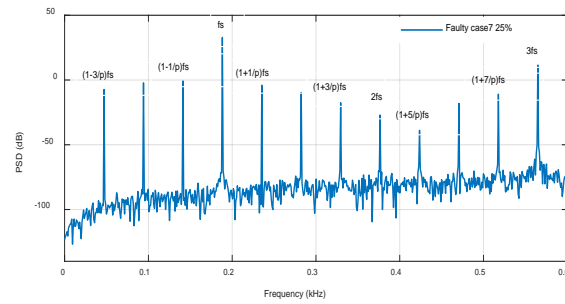- Case 6: Uniform reduction of a single B_{PM} magnet
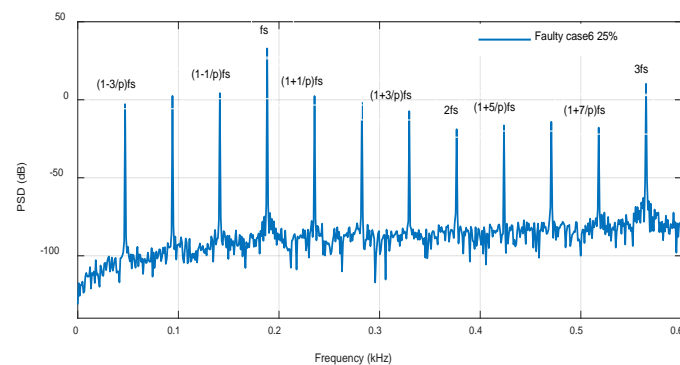
(a)

(b)

Figure 28. *Cont.*

(**c**)

Figure 28. Faulty case 6: (**a**) PMSM current spectra normalized plot under 25%; (**b**) PMSM current spectra normalized plot under 75%; (**c**) ASBCs harmonics variations.

- Case 7: Symmetric reduction of a single B_{PM} magnet

(**a**)

(**b**)

(**c**)

Figure 29. Faulty case 7: (**a**) PMSM current spectra normalized plot under 25%; (**b**) PMSM current spectra normalized plot under 75%; (**c**) ASBCs harmonics variations.

- Case 8: Asymmetric reduction of a single B_{PM} magnet
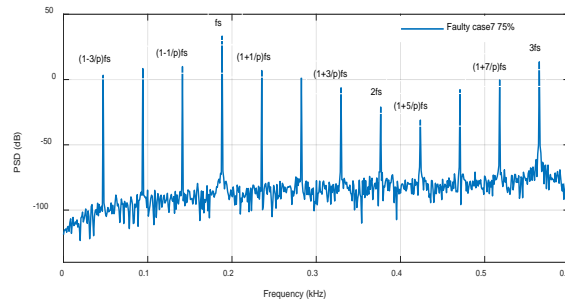

(a)

(b)
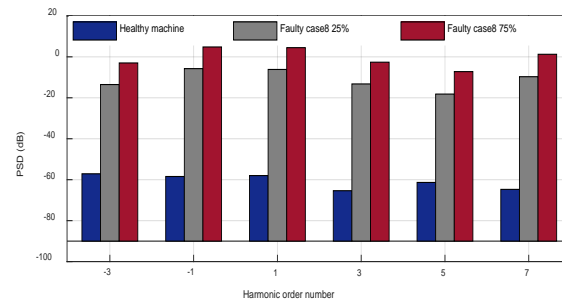
(c)

Figure 30. Faulty case 8: (**a**) PMSM current spectra normalized plot under 25%; (**b**) PMSM current spectra normalized plot under 75%; (**c**) ASBCs harmonics variations.

- Case 9: Symmetric reduction of a single PM arc angle

(a)

Figure 31. *Cont.*

(**b**)

(**c**)

Figure 31. Faulty case 9: (**a**) PMSM current spectra normalized plot under 25%; (**b**) PMSM current spectra normalized plot under 75%; (**c**) ASBCs harmonics variations.
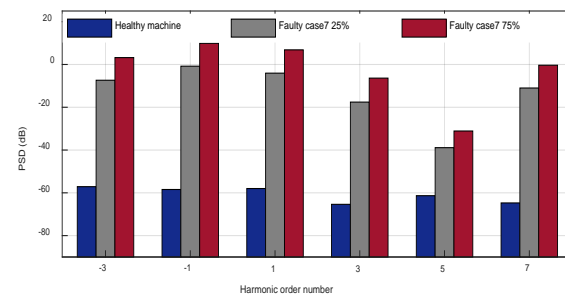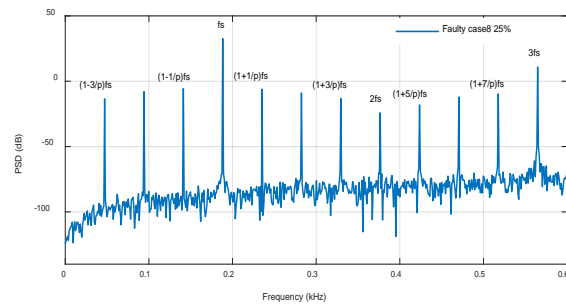
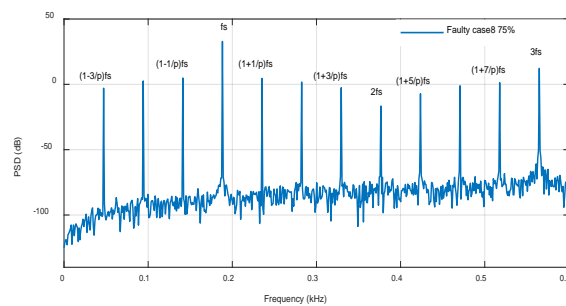- Case 10: Asymmetric reduction of a single PM arc magnet

(**a**)

(**b**)

Figure 32. *Cont.*

(**c**)

Figure 32. Faulty case 10: (**a**) PMSM current spectra normalized plot under 25%; (**b**) PMSM current spectra normalized plot under 75%; (**c**) ASBCs harmonics variations.
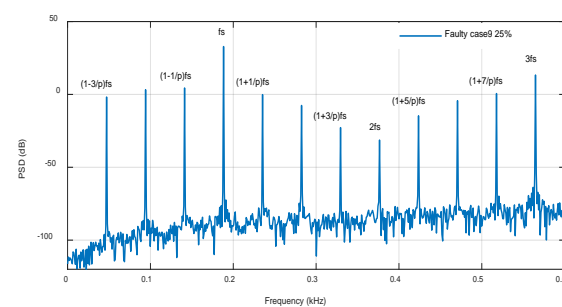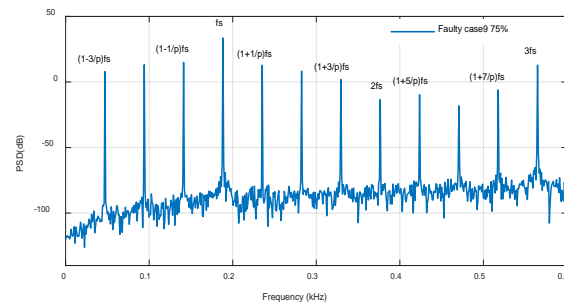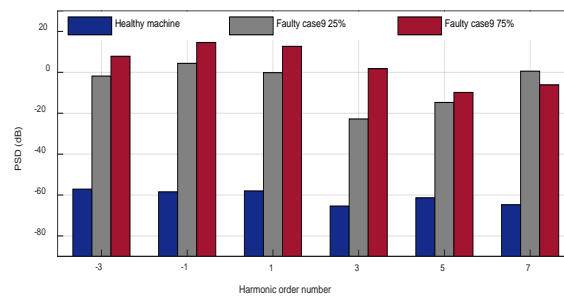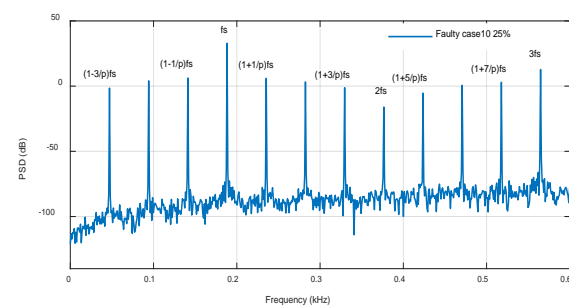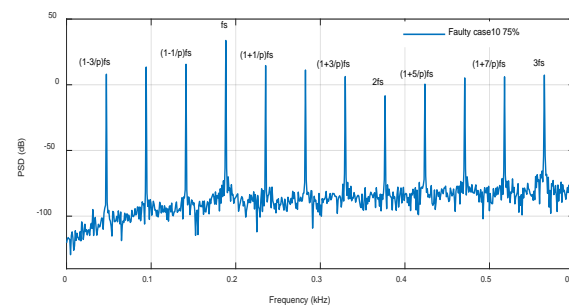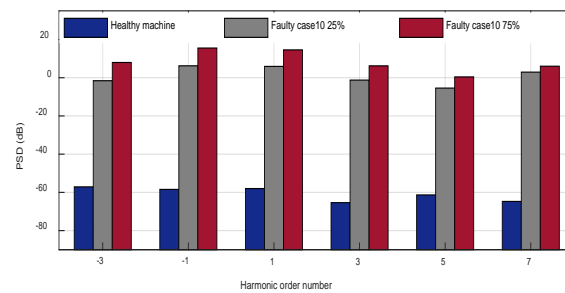
4.3.2. MCSA Results Analysis under Partial Demagnetization

For the studied PMSM, the data exhibit that the fault signature patterns induced by several partial demagnetized PM fault types generate different features in the current signal that could be used to recognize defect types.

The results in Figures 28–32 and detailed in Tables 6–10, prove that the existence of a local DMF produces additional even harmonics in the stator current spectrum, as predicted in (6). As seen in these Figures and Tables, the higher degree fault enhances the ASBCs. Its observation could make it possible to recognize the type of defect in demagnetization.

It has been shown that the local DMF can be clearly diagnosed using these harmonic components, but a uniform DMF does not produce asymmetry and, consequently, there is no unbalance and the harmonic component will not exist in the motor. Thus, the current harmonics composition analysis does not have obvious results to a uniform DMF. Based on the above, the MCSA method is invalid to detect and diagnose a PMSM uniform DMF.

Table 6. Current harmonic components comparison due to case 6 (in dB).

Frequency	Healthy Machine	Faulty Case 6 25%	Faulty Case 6 75%
$(1-3/\text{P})f_s$	−57.12	−02.86	07.93
$(1-1/\text{P})f_s$	−58.44	04.22	15.16
$(1+1/\text{P})f_s$	−57.99	02.32	13.48
$(1+3/\text{P})f_s$	−65.38	−07.36	03.91
$(1+5/\text{P})f_s$	−61.34	−16.51	−04.36
$(1+7/\text{P})f_s$	−64.73	−17.91	−04.30

Table 7. Current harmonic components comparison due to case 7 (in dB).

Frequency	Healthy Machine	Faulty Case 7 25%	Faulty Case 7 75%
$(1-3/\text{P})f_s$	−57.12	−07.37	03.21
$(1-1/\text{P})f_s$	−58.44	−00.79	09.88
$(1+1/\text{P})f_s$	−57.99	−04.05	06.83
$(1+3/\text{P})f_s$	−65.38	−17.59	−06.37
$(1+5/\text{P})f_s$	−61.34	−38.89	−31.10
$(1+7/\text{P})f_s$	−64.73	−11.00	−00.34

Table 8. Current harmonic components comparison due to case 8 (in dB).

Frequency	Healthy Machine	Faulty Case 8 25%	Faulty Case 8 75%
$(1-3/\text{P})f_s$	−57.12	−13.53	−02.99
$(1-1/\text{P})f_s$	−58.44	−05.75	04.81
$(1+1/\text{P})f_s$	−57.99	−06.16	04.48
$(1+3/\text{P})f_s$	−65.38	−13.24	−02.62
$(1+5/\text{P})f_s$	−61.34	−18.19	−07.21
$(1+7/\text{P})f_s$	−64.73	−09.70	01.24

Table 9. Current harmonic components comparison due to case 9 (in dB).

Frequency	Healthy Machine	Faulty Case 9 25%	Faulty Case 9 75%
$(1-3/\text{P})f_s$	−57.12	−01.82	07.86
$(1-1/\text{P})f_s$	−58.44	04.39	14.90
$(1+1/\text{P})f_s$	−57.99	−00.15	12.71
$(1+3/\text{P})f_s$	−65.38	−22.80	01.82
$(1+5/\text{P})f_s$	−61.34	−14.72	−09.82
$(1+7/\text{P})f_s$	−64.73	00.56	−06.09

Table 10. Current harmonic components comparison due to case 10 (in dB).

Frequency	Healthy Machine	Faulty Case 10 25%	Faulty Case 10 75%
$(1-3/\text{P})f_s$	−57.12	−01.57	07.97
$(1-1/\text{P})f_s$	−58.44	06.23	15.53
$(1+1/\text{P})f_s$	−57.99	05.92	14.56
$(1+3/\text{P})f_s$	−65.38	−01.24	06.21
$(1+5/\text{P})f_s$	−61.34	−05.42	00.42
$(1+7/\text{P})f_s$	−64.73	02.92	06.02

5. Conclusions

This work has presented a FEA modeling investigation of a PMSM running under a set of various PM defects to extract, analyze, and correlate the fault signatures resulting from distinct predefined fault cases. One of the main reasons for diagnosing a demagnetization defect at the initial stage of its occurrence is the growing cost of NdFeB PMs and the need for a cost-effective condition monitoring in various industrial applications.

A study has been performed that links possible current spectral signature models to the nature of the PM field distortion resulting from a particular PM demagnetization defect. A mathematical characterization of the disturbance of the idealized airgap field created by a particular case of demagnetization was used as an initial reference base to understand the possible diagnostic content in the current spectrum, before exploring the predictions using the FEA model. It is worth noticing that, while different demagnetization defects of PMs give rise to almost similar characteristics in the stator current spectrum, specific signature characteristics could be identified in certain cases, which allow a fault classification and localization for different demagnetization defects.

Possible PM demagnetization faults have been simulated based on the finite element method. Current signatures are evaluated adopting an FEA model and numeric values of individual harmonic orders are obtained from the spectrum of the stator current. Available indices for the detection of a demagnetization fault are introduced. In some fault cases, these indices make it possible to determine the degree of fault as a function of the level of the harmonics. Unfortunately, in the case of a uniform damage, there are no additional harmonics generated by the fault in the stator current. Thus, this index is not able to detect the type of defect and the MCSA is not a valid method for detecting the defect of uniform demagnetization. Consequently, it is necessary in the future scope to find an efficient technique to diagnose uniform demagnetization.

The detailed description of different cases of the demagnetization fault as well as the obtained numerical results will be used as a platform for intelligent and more advanced diagnostic methods, which will be investigated in future works.

Author Contributions: Conceptualization, M.K., E.E., and M.B.; Methodology, M.K., E.E., and M.B.; Software, M.K.; Validation, M.K., E.E., N.B., M.C., M.B., and R.N.; Formal Analysis, M.K., E.E., and M.B.; Investigation, M.K.; Writing—Original draft preparation, M.K.; Writing—review & editing, M.K., E.E., N.B., M.C., M.B., and R.N. All authors have read and agreed to the published version of the manuscript.

Nomenclature

PMSM	Permanent magnet synchronous motor
DMF	Demagnetization fault
ISCF	Inter turn short-circuit fault
PM	Permanent magnet
SE	Static eccentricity
PMSLM	Permanent magnet synchronous linear motor
FFT	Fast Fourier transform
MCSA	Motor current signature analysis
VKF-OT	Vold-Kalman filtering order tracking
HHT	Hilbert-Huang transform
1D CNN	1D conventional neural network
DBN	Dynamic Bayesian network
ST	S-transform
PSO–LSSVM	Particle swarm optimization–least squares support vector machine
DPMSLM	Double-side permanent magnet synchronous linear motor
ELM	Extreme Learning Machine
MMF	Magnetomotive force
ASBC	Amplitude of sideband component
PSD	Power spectral density
NdFeB	Neodymium-boron
UMP	Unbalanced magnetic pull
EMF	Electromotive force
FEM	Finite element method
θ_r	Rotor angular position
f_s	Synchronous electrical frequency
f_{UD}	Uniform demagnetization frequency
f_{LD}	Local demagnetization frequency
B	Healthy rotor magnetic flux density distribution
B_{UD}	Uniform demagnetized rotor magnetic flux density distribution
B_{PM}	PM flux density
α_M	Magnet arc angle
p	Pole-pairs number
M	Flux density magnitude fault severity indices
X	Magnet arc angle fault severity indices
dB	Decibel
T	Tesla

Appendix A

Table A1. PMSM Parameters.

Designation	Value	Unit
Core stack length	250	mm
Rotor exterior diameter	82	mm
Stator interior diameter	102	mm
Stator exterior diameter	174	mm
Poles number	8	-
Slots number	12	-
Magnets number	8	-
Magnet height	7.76	mm
Magnet coercivity	8.95×10^5	A/m
Magnet remanence	1.1	T
Terminal current	59.5	A
Power shaft	62	KW
Supply frequency	188.3	Hz
Rotational speed	2824	rpm

References

1. Rosero, J.; Romeral, L.; Ortega, J.A.; Urresty, J.C. Demagnetization fault detection by means of Hilbert Huang transform of the stator current decomposition in PMSM. *IEEE Int. Symp. Ind. Electron.* **2008**, 172–177. [CrossRef]

2. Faiz, J.; Mazaheri-Tehrani, E. Demagnetization modeling and fault diagnosing techniques in permanent magnet machines under stationary and nonstationary conditions: An overview. *IEEE Trans. Ind. Appl.* **2016**, *53*, 2772–2785. [CrossRef]

3. Ruschetti, C.; Verucchi, C.; Bossio, G.; De Angelo, C.; García, G. Rotor demagnetization effects on permanent magnet synchronous machines. *Energy Conv. Manag.* **2013**, *74*, 1–8. [CrossRef]

4. Manel, K.; Mohamed, C.; Elhoussin, E.; Naourez, B.H.; Benbouzid, M.E.H.; Rafik, N. Eccentricity Faults Diagnosis in Permanent Magnet Synchronous Motors: A Finite Element-Based Approach. *Int. J. Energy Conv. (IRECON)* **2019**, *7*. [CrossRef]

5. Mazaheri-Tehrani, E.; Faiz, J.; Zafarani, M.; Akin, B. A Fast Phase Variable abc Model of Brushless PM Motors Under Demagnetization Faults. *IEEE Trans. Ind. Electron.* **2018**, *66*, 5070–5080. [CrossRef]

6. Choi, G.; Jahns, T.M. Post-demagnetization characteristics of permanent magnet synchronous machines. In Proceedings of the IEEE Energy Conversion Congress and Exposition (ECCE), Montreal, QC, Canada, 20–24 September 2015; pp. 1781–1788.

7. Alwadie, A. The decision making system for condition monitoring of induction motors based on vector control model. *Machines* **2017**, *5*, 27. [CrossRef]

8. Ullah, Z.; Hur, J. A comprehensive review of winding short circuit fault and irreversible demagnetization fault detection in pm type machines. *Energies* **2018**, *11*, 3309. [CrossRef]

9. Faiz, J.; Nejadi-Koti, H. Demagnetization fault indexes in permanent magnet synchronous motors—An overview. *IEEE Trans. Magn.* **2015**, *52*, 1–11. [CrossRef]

10. Chen, Y.; Liang, S.; Li, W.; Liang, H.; Wang, C. Faults and Diagnosis Methods of Permanent Magnet Synchronous Motors: A Review. *Appl. Sci.* **2019**, *9*, 2116. [CrossRef]

11. Fico, V.M.; Rodríguez Vázquez, A.L.; Martín Prats, M.Á.; Bernelli-Zazzera, F. Failure Detection by signal similarity measurement of Brushless DC motors. *Energies* **2019**, *12*, 1364. [CrossRef]

12. Manel, K.; Mohamed, C.; Naourez, B.H.; Rafik, N. Fault Detection and Diagnosis Methods in Permanent Magnet Synchronous Machines: A Review. In Proceedings of the International Conference on Recent Advances in Electrical System (ICRAES'17), Hammamet, Tunisia, 22–24 December 2017.

13. Isermann, R. Model-based fault-detection and diagnosis–status and applications. *Ann. Rev. Control* **2005**, *29*, 71–85. [CrossRef]

14. Bellini, A.; Filippetti, F.; Tassoni, C.; Capolino, G.A. Advances in diagnostic techniques for induction machines. *IEEE Trans. Ind. Electron.* **2008**, *55*, 4109–4126. [CrossRef]

15. Wang, C.; Prieto, M.D.; Romeral, L.; Chen, Z.; Blaabjerg, F.; Liu, X. Detection of partial demagnetization fault in PMSMs operating under non stationary conditions. *IEEE Trans. Magn.* **2016**, *52*, 1–4.

16. Zhu, M.; Yang, B.; Hu, W.; Feng, G.; Kar, N.C. Vold-Kalman Filtering Order Tracking Based Rotor Demagnetization Detection in PMSM. *IEEE Trans. Ind. Appl.* **2019**, *55*, 5768–5778. [CrossRef]

17. Zhang, J.; Tounzi, A.; Benabou, A.; Le Menach, Y. Detection of magnetization loss in a PMSM with Hilbert Huang transform applied to non-invasive search coil voltage. *Math. Comp. Sim.* **2020**. [CrossRef]

18. Moon, S.; Lee, J.; Jeong, H.; Kim, S.W. Demagnetization fault diagnosis of a PMSM based on structure analysis of motor inductance. *IEEE Trans. Ind. Electron.* **2016**, *63*, 3795–3803. [CrossRef]

19. Lee, H.; Jeong, H.; Kim, S.W. Detection of Interturn Short-Circuit Fault and Demagnetization Fault in IPMSM by 1-D Convolutional Neural Network. In Proceedings of the IEEE PES Asia-Pacific Power and Energy Engineering Conference (APPEEC), Macao, China, 1–4 December 2019; pp. 1–5.

20. Moon, S.; Jeong, H.; Lee, H.; Kim, S.W. Detection and classification of demagnetization and interturn short faults of IPMSMs. *IEEE Trans. Ind. Electron.* **2017**, *64*, 9433–9441. [CrossRef]

21. Haddad, R.Z.; Lopez, C.A.; Foster, S.N.; Strangas, E.G. A voltage-based approach for fault detection and separation in permanent magnet synchronous machines. *IEEE Trans. Ind. Appl.* **2017**, *53*, 5305–5314. [CrossRef]

22. Nejadi-Koti, H.; Faiz, J.; Demerdash, N.A. Uniform demagnetization fault diagnosis in permanent magnet synchronous motors by means of cogging torque analysis. In Proceedings of theIEEE International Electric Machines and Drives Conference (IEMDC), Miami, FL, USA, 21–24 May 2017; pp. 1–7.

23. Gao, C.; Nie, Y.; Si, J.; Fu, Z.; Feng, H. Mode Recognition and Fault Positioning of Permanent Magnet Demagnetization for PMSM. *Energies* **2019**, *12*, 1644. [CrossRef]

24. Ishikawa, T.; Igarashi, N. Failure Diagnosis of Demagnetization in Interior Permanent Magnet Synchronous Motors Using Vibration Characteristics. *Appl. Sci.* **2019**, *9*, 3111. [CrossRef]

25. Song, X.; Zhao, J.; Song, J.; Dong, F.; Xu, L.; Zhao, J. Local Demagnetization Fault Recognition of Permanent Magnet Synchronous Linear Motor based on S-transform and PSO-LSSVM. *IEEE Trans. Power Electron.* **2020**, *35*, 7816–7825. [CrossRef]

26. Toumi, S.; Elbouchikhi, E.; Amirat, Y.; Benbouzid, M.; Feld, G. Magnet failure-resilient control of a direct-drive tidal turbine. *Ocean Eng.* **2019**, *187*, 106207. [CrossRef]

27. Song, J.; Zhao, J.; Dong, F.; Zhao, J.; Xu, L.; Yao, Z. A New Demagnetization Fault Recognition and Classification Method for DPMSLM. *IEEE Trans. Ind. Inf.* **2019**, *16*, 1559–1570. [CrossRef]

28. Elbouchikhi, E.; Choqueuse, V.; Auger, F.; Benbouzid, M.E.H. Motor current signal analysis based on a matched subspace detector. *IEEE Trans. Inst. Meas.* **2017**, *66*, 3260–3270. [CrossRef]

29. Melecio, J.I.; Djurović, S.; Schofield, N. FEA model study of spectral signature patterns of PM demagnetization faults in synchronous PM machines. *J. Eng.* **2019**, *17*, 4127–4132.

30. Quintal-Palomo, R.E. Analysis of Current Signals in a Partially Demagnetized Vector Controlled Interior Permanent Magnet Generator. *Power Electron. Drives* **2019**, *4*, 179–190. [CrossRef]

31. Alameh, K.; Cité, N.; Hoblos, G.; Barakat, G. Vibration-based fault diagnosis approach for permanent magnet synchronous motors. *IFAC* **2015**, *48*, 1444–1450. [CrossRef]

32. Zafarani, M.; Goktas, T.; Akin, B. A comprehensive magnet defect fault analysis of permanent-magnet synchronous motors. *IEEE Trans. Ind. Appl.* **2015**, *52*, 1331–1339.